Unified Boundary Trapezoidal Modulation Control Utilizing Fixed Duty Cycle Compensation and Magnetizing Current Design for Dual Active Bridge DC–DC Converter

Guo Xu, *Student Member, IEEE*, Deshang Sha, *Member, IEEE*, Jiankun Zhang, and Xiaozhong Liao, *Member, IEEE*

***Abstract*—The unified boundary trapezoidal modulation (TZM) control utilizing fixed duty cycle compensation and magnetizing current design for dual active bridge dc–dc converter is proposed in this paper. The fixed duty cycle compensation and magnetizing current design are first introduced to achieve the zero voltage switching (ZVS) of the power switches, which cannot be ensured with the conventional TZM control. As a result, all the power switches of dual active dc–dc converter can achieve ZVS and four switches can be turned off with very low current. Besides, based on the revealed power transfer characteristic, the power control variables including the duty cycles and phase-shift ratio can be unified without lookup tables or operation region division. With the proposed boundary TZM control, circulating current losses can be reduced and nonactive power is significantly suppressed according to the mathematic analysis, resulting in decrease of the conduction loss. A 1.6-kW laboratory prototype is built to verify the theoretical analysis and effectiveness of the proposed control.**

***Index Terms*—Boundary trapezoidal modulation (boundary TZM control), dual active bridge, fixed duty cycle compensation, zero voltage switching (ZVS).**

I. Introduction

THE dual-active-bridge (DAB) dc–dc converter, consisting of two active bridges and a high-frequency transformer, is first proposed in early 1990s [1], [2]. Nowadays, it has become a preferred topology for power conversion applications that require galvanic isolation and bidirectional power flow due to its many advantages, such as high-power density, bidirectional power transfer capability, zero-voltage switching (ZVS) and symmetric structure.

The conventional phase-shift (CPS) technique [3]–[5] is a simple way to regulate the power flow of DAB converters, since the waveforms of the two voltages generated by the two active bridges are both square waves with 50% duty ratio and it only controls the phase-shift ratio between the two voltages. Under CPS control, the unified control can be realized just by the implementation of a PI regulator. However, when the voltage conversion ratio varies, the conversion efficiency could be limited because of the conduction loss due to the high nonactive power and the switching loss caused by limited ZVS ranges [6]. Meanwhile, it has been pointed out that the nonactive power with CPS control is the main factor contributing to large peak current and large conduction loss [7]. The extended-phase-shift (EPS) control [8]–[10] is a typical improvement of CPS since the inner phase-shift ratio of one active bridge is added as another control degree of freedom to extend the ZVS operation range and also reduce the conduction loss. To further reduce the conduction loss and improve the performance of DAB converter, both of the two inner phase-shift ratios (also called as two duty cycles) for the two active bridges can be regulated, such as dual-phase-shift (DPS) [7], [11], [12] and phase-shift plus pulse width modulation (PSPWM) control [13]–[15]. PSPWM control can also be called triple phase-shift (TPS) control as it needs to control three degrees of freedom, including the phase-shift ratio of the two bridges and two duty cycles. Actually, CPS, EPS, and DPS can be regarded as the special case of TPS. Although TPS can lead to optimized operation, it is complex since the power transfer depends on three independent control variables. The selections of these control variables are very difficult to be unified and are usually relied on a lookup table stored in computer memory due to the complex calculation.

The nonactive current [7], [16], [17] causes additional conduction loss for DAB converters. The nonactive power loss is defined in [17] and used as the optimization object to reduce the conduction loss with TPS control. However, the selection of the control variables is also not unified and hard to be implemented in real time calculation. To reduce non-active power, the triangular modulation (TRM) [18], [19] has no nonactive power issue and can achieve zero current switching (ZCS) for four switches. But the ZVS is lost for these ZCS switches. Even though the modified TRM control is proposed in [20] and [21], it still suffers from high-peak current and large rms current. These issues can be avoided with the hybrid modulation [20] using CPS at heavy load and the modified TRM control at light load. While smooth transfer between the two modes is a challenge. Compared with TRM, the trapezoidal modulation (TZM)

Manuscript received November 29, 2015; revised March 9, 2016; accepted April 11, 2016. Date of publication April 20, 2016; date of current version December 9, 2016. This work was supported in part by the National Natural Science Foundation of China under Grant 51577012, in part by the Program for New Century Excellent Talents in University of China under Grant NCET-13-0043, Technology Foundation for Selected Overseas Chinese Scholar (2014), by the Ministry of Human Resources and Social Security of China, and by the 2016 Fundamental Research Fund of Beijing Institute of Technology. Recommended for publication by Associate Editor G. Moschopoulos. *(Corresponding author: Deshang Sha.)*

The authors are with the Advanced Power Conversion Center, School of Automation, Beijing Institute of Technology, Beijing 100081, China (e-mail: xuguobit@bit.edu.cn; shadeshang@bit.edu.cn; backpacker47@bit.edu.cn; liaoxiaozhong@bit.edu.cn).

Color versions of one or more of the figures in this paper are available online at http://ieeexplore.ieee.org.

Digital Object Identifier 10.1109/TPEL.2016.2555328

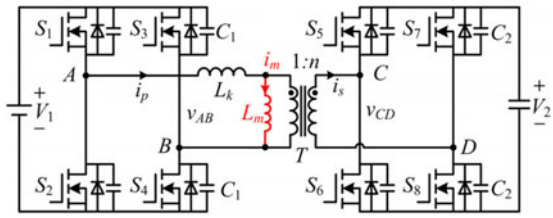

Fig. 1. Topology of DAB dc–dc converter.

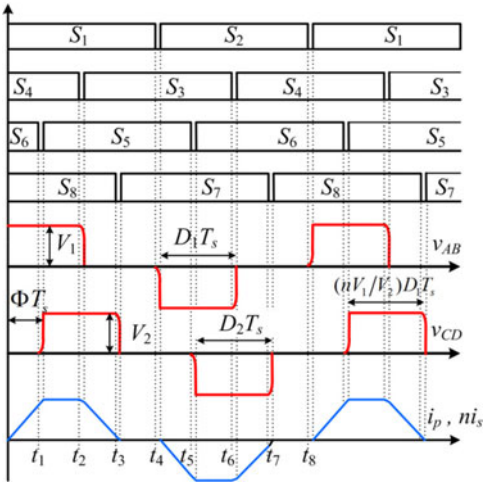

Fig. 2. Typical operation waveform of TZM.

[19] can make the active bridge work with large duty cycles and result in lower peak current and rms value. Meanwhile, compared with the CPS, EPS, and DPS, nonactive current is avoided. Although the operation principle of TZM has been discussed extensively in the literature, how to select the two control variables including duty cycle and phase-shift ratio in an optimized way has not been discussed yet. Besides, the ZVS of four power switches cannot be achieved since the transformer leakage current maintains zero when the power switches are turned OFF.

A unified boundary TZM control utilizing fixed duty cycle compensation and magnetizing current design for dual active bridge dc–dc converter is proposed in this paper. This unified control can be implemented by one regulator based on the introduced boundary condition of TZM control. The fixed duty cycle compensation and magnetizing current design are proposed to achieve ZVS of the left four power switches, which cannot be obtained for the converter with conventional TZM. With this unified boundary control, ZVS of all the power switches can be achieved and four switches can almost achieve ZCS. Meanwhile, the control strategy is unified and the nonactive current can be minimized significantly.

This paper is organized as follows. The proposed fixed duty cycle compensation and magnetizing current design based on the ZVS analysis are discussed in Section II. According to the power transfer characteristic, the unified control based on selection for duty cycles and phase-shift ratio is presented in Section III. Section IV introduces the implementation of the boundary control. The experimental results are given in Section V. Finally, the conclusion is made in Section VI.

II. Fixed Duty Cycle Compensation and Magnetizing Current Design for DAB DC–DC Converter with TZM

Fig. 1 shows the topology of DAB dc–dc converter. It consists of two active bridges connected by a high-frequency transformer. The active bridge in the left side generates a high-frequency voltage v_{AB}, and the other one generates voltage v_{CD}. Bidirectional power transfer is controlled by the phase-shift ratio between the two high-frequency voltages and their duty cycles.

A. Conventional TZM

The operation principle of TZM is introduced in Fig. 2. Φ is the phase-shift ratio between the voltages generated by two active bridges, and D_1 and D_2 represent the inner phase-shift ratio of the two active bridges, respectively, which are also named as duty cycles. T_s is the switching period and 1: n denotes the transformer turns ratio. i_p and i_s are the transformer currents in V_1 and V_2 sides, respectively, which are also denoted in Fig. 1. Unlike CPS and EPS control, neither D_1 nor D_2 are fixed as 0.5. They are both less than 0.5 and can be different when V_1 is not equal to V_2/n. The relationship of D_1 and D_2 for TZM is written as [21]

$$D_2 = (nV_1/V_2)D_1. \tag{1}$$

The power transfer under TZM is also given as

$$P_o{}^{\mathrm{TZM}} = \frac{V_1}{L_k f_s}(D_1{}^2 V_1 - (D_1 - \Phi)^2 V_2/n) \tag{2}$$

where f_s is the switching frequency. Compared with CPS, EPS and other control method, TZM has its unique advantages such as no nonactive power, ZCS, and changeable duty cycles when the input and output voltage is not matched.

B. ZVS Conditions for DAB Converter with Conventional TZM Control

To achieve ZVS of power switches for a conventional full bridge converter with phase-shift control, the energy in the inductive components must be high enough to charge/discharge their junction capacitors completely. The dead time of the two switches in the same leg should also be properly designed to ensure that the charge/discharge process is finished before switches are turned ON. This principle is also applied to TZM DAB converter. Just like the conventional full bridge converter, the switches in the lagging leg can achieve ZVS easily because the transformer leakage current is almost approaching its maximum value before these switches are turned ON. As for the leading leg switches, the transformer leakage current is always zero when the switches are turned OFF if the magnetizing current is ignored. ZVS is impossible as there is no current to charge/discharge the junction capacitors. Consequently, for

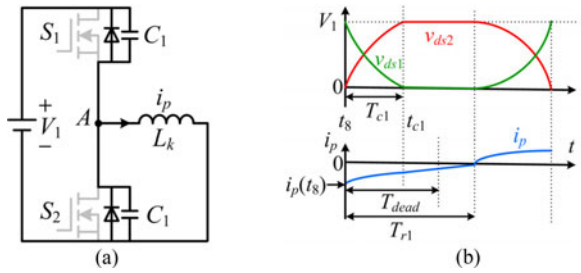

Fig. 3. ZVS conditions for S1 and S2. (a) Circuit. (b) Waveforms.

TZM DAB converter, S_3, S_4, S_5, and S_6 can achieve ZVS, while S_1, S_2, S_7, and S_8 cannot [19].

The leg composed of S_1 and S_2 is taken as an example to analyze ZVS conditions for these leading legs, as shown in Fig. 3. Because the two switches are the same type, the junction capacitors are both denoted as C_1 in Fig. 3. When S_2 is turned OFF at time t_8 (t_8 is denoted in Fig. 2), none of the two switches conducts and the secondary side of the transformer is shorted. The corresponding equivalent circuit is shown in Fig. 3(a) and related current and voltage waveforms after t_8 are shown in Fig. 3 (b).

To charge/discharge the junction capacitors, the energy stored in the inductor L_k should be larger than that in the two capacitors

$$0.5L_k{i_p}^2(t_8) \geq 0.5C_1{V_1}^2 + 0.5C_1{V_1}^2. \tag{3}$$

The current should charge the junction capacitor of S_2 before S_1 is turned ON. Therefore, $i_{p(t_8)} < 0$. According to (3), it can be written by

$$i_p(t_8) \leq -V_1\sqrt{2C_1/L_k}. \tag{4}$$

Meanwhile, according to the circuit in Fig. 3(a), the relationship of i_p and v_{ds2} is

$$\begin{cases} L_k di_p/dt = v_{ds2} \\ i_p = C_1 d(V_1 - v_{ds2})/dt - C_1 dv_{ds2}/dt = -2C_1 dv_{ds2}/dt \end{cases} \tag{5}$$

where v_{ds1} and v_{ds2} are the junction voltage for S_1 and S_2, respectively.

The initial value of v_{ds2} is

$$v_{ds2}(t_8) = 0. \tag{6}$$

Based on (5) and (6), v_{ds2} can be expressed as

$$v_{ds2}(t - t_8) = \frac{-i_p(t_8)}{\sqrt{2C_1/L_k}} \sin\frac{t - t_8}{\sqrt{2C_1L_k}}. \tag{7}$$

The charging process is not finished until v_{ds2} reaches its maximum value V_1. Based on (7), the charging time T_{c1} can be written by

$$T_{c1} = t_{c1} - t_8 = \sqrt{2C_1L_k}\arcsin[-V_1\sqrt{2C_1/L_k}/i_p(t_8)]. \tag{8}$$

S_1 should be turned ON after the charging process is over. Meanwhile, when i_p reaches zero, the junction capacitor of S_2 starts to discharge, causing loss of ZVS. As a result, S_1 should be turned ON before i_p reaches zero. Therefore, as also illustrated in Fig. 3(b)

$$T_{c1} < T_{\text{dead1}} < T_{r1}. \tag{9}$$

Based on (7)

$$i_p(t_{c1}) = -2C_1\frac{dv_{ds2}}{dt}(t_{c1}) = i_p(t_8)\cos\left[(t_{c1} - t_8)/\sqrt{2C_1L_k}\right). \tag{10}$$

Since $L_k i_p(t_{c1})/T_{r1} = V_1$, T_{r1} can be expressed as

$$T_{r1} = \frac{V_1}{L_k i_p(t_8)\cos(T_{c1}/\sqrt{2C_1L_k})} + T_{c1}. \tag{11}$$

To sum up, the minimum current for achieving ZVS of S_1 has been illustrated in (4). The limit for the dead time is also given in (8), (9), and (11).

Likewise, ZVS conditions for the other three switches (S_2, S_7, S_8) can also be summed up in Table I. t_3, t_4, t_7, and t_8 are the switch turn OFF instants denoted in Fig. 2; C_2 is the junction capacitor of switch S_7 or S_8; $L_{ks} = n^2L_k$, which is the equivalent transformer leakage inductance of V_2 side reflected from V_1 side.

C. Proposed Fixed Duty Cycle Compensation

The proposed fixed duty cycle compensation is shown in Fig. 4 to achieve ZVS for S_1 and S_2. As illustrated, instead of using the relationship of duty cycles in (1), a duty cycle compensation value D_c is added and expressed as

$$D_2 = (nV_1/V_2)D_1 - D_c. \tag{12}$$

As shown in Fig. 4, unlike the conventional TZM method, a bias current (I_b) occurs in i_p at the moment (t_4 or t_8) when S_1 or S_2 turns OFF. If this bias current is properly designed, it can be used to charge/discharge the junction capacitor to achieve ZVS.

Since phase-shift control is used, the polarity of the bias current during the interval $t_3 - t_4$ should be reversed with the one during interval $t_7 - t_8$. The relationship of $i_{(p)(t_8)}$ and $i_{(p)(t_3)}$ can be expressed as

$$i_p(t_3) = -i_p(t_8) = I_b. \tag{13}$$

Meanwhile, $i_{(p)(t_3)}$ can also be calculated as

$$i_p(t_3) = T_s(D_1V_1 - D_2V_2/n)/L_k - I_b. \tag{14}$$

Substitution of (12) and (13) into (14) yields

$$I_b = D_cT_sV_2/(2nL_k). \tag{15}$$

According to the ZVS conditions in the previous section, to achieve ZVS for S_1 and S_2, the bias current must be larger than the minimum charge current

$$I_b > I_{1\min} = V_1\sqrt{2C_1/L_k}. \tag{16}$$

Then based on (15) and (16), D_c should be design as

$$D_c > 2nV_1\sqrt{2C_1L_k}/(T_sV_2). \tag{17}$$

Equation (17) shows that a minimum duty cycle compensation value D_c can be designed to achieve ZVS for S_1 and S_2

TABLE I
ZVS CONDITIONS FOR THE FOUR SWITCHES

	S_1	S_2	S_7	S_8
Current range	$i_p(t_8) < -I_{1\min}$	$i_p(t_4) > I_{1\min}$	$i_s(t_3) < -I_{2\min}$	$i_s(t_7) > I_{2\min}$
Dead time	$T_{c1} < T_{dead1} < T_{r1}$		$T_{c2} < T_{dead2} < T_{r2}$	

$$T_{c2} = \sqrt{2C_2 L_{ks}} \arcsin \frac{V_2\sqrt{\frac{2C_2}{L_{ks}}}}{-i_s(t_3)},\ t_{r2} = \frac{V_2}{L_{ks} i_s(t_3) \cos \frac{T_{c2}}{\sqrt{2C_2 L_{ks}}}} + T_{c2},\ I_{2\min} = V_2\sqrt{\frac{2C_2}{L_{ks}}},\ I_{1\min} = V_1\sqrt{\frac{2C_1}{L_k}}$$

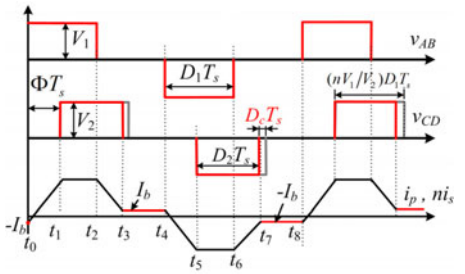

Fig. 4. Fixed duty cycle compensation.

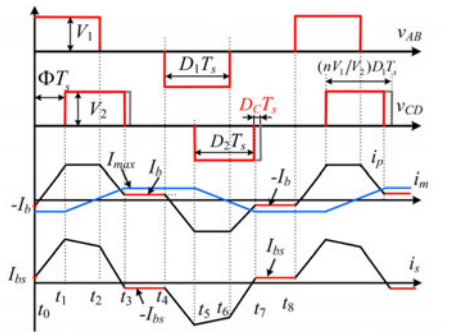

Fig. 5. Magnetizing current design to achieve ZVS for S_7 and S_8.

regardless of the load. This implies the ZVS achievement is not affected by the output power. It is worth noting that the dead time can be designed according to its limit in Table I.

D. Magnetizing Current Design to Achieve ZVS for S_7 and S_8

In the literature, the magnetizing current of the transformer is seldom considered for nonresonant DAB converters. Based on Table I, to achieve ZVS of S_2, $i_{(p)(t_4)} > I_{1\min}$; while to achieve ZVS for S_7, $i_{(s)(t_3)} < -I_{2\min}$. However, when the magnetizing current is ignored, $i_{(p)(t_4)} = ni_{s(t_3)}$, which is illustrated in both Figs. 2 and 3. This leads to a conflict between ZVS conditions of S_2 and S_7, resulting in that only one of the two switches can achieve ZVS. Similarly, the conflict also exists between ZVS for S_1 and S_6. As a result, although ZVS of S_1 and S_2 can be achieved with the proposed duty cycle compensation, ZVS of S_7 and S_8 still cannot be obtained. To obtain the ZVS conditions: $i_{s|t=t3} < -I_{2\min}$ and $i_{s|t=t7} < -I_{2\min}$ for S_7 and S_8, the magnetizing current i_m can be utilized as shown in Fig. 5.

Fig. 5 illustrates the waveforms of i_p, the magnetizing current i_m, and i_s utilizing the magnetizing current. In this case, the waveform of i_p is the same as the one shown in Fig. 4, while the value of ni_s is written by

$$ni_s = i_p - i_m \tag{18}$$

where n is the turns ratio as mentioned before, and ni_s is the current of transformer in V_2 side reflected to V_1 side.

As shown in Fig. 5, at t_3, i_m is equal to $I_{\max}$, and the following can be obtained during interval $t_1 - t_3$:

$$L_m \frac{2I_{\max}}{D_2 T_s} = \frac{V_2}{n}. \tag{19}$$

Rearranging (19) yields

$$I_{\max} = V_2 D_2 T_s / (2nL_m). \tag{20}$$

At t_3, the bias current of i_s can be expressed as

$$I_{bs} = -(I_b - I_{\max})/n. \tag{21}$$

Substituting (20) into (21), the expression of the current bias I_{bs} for V_2 side can be obtained as

$$I_{bs} = V_2 D_2 T_s/(2n^2 L_m) - I_b/n \tag{22}$$

where the expression of I_b is shown in (15).

To design a suitable bias current I_{bs} in order to obtain ZVS for S_7 and S_8 in Table I, its value is written by

$$I_{bs} = V_2 D_2 T_s/(2n^2 L_m) - I_b/n > I_{2\min}. \tag{23}$$

Once I_{bs} is certain, the dead time can also be designed according to the dead time limit in Table I.

III. POWER TRANSFER CHARACTERISTIC AND SELECTIONS OF DUTY CYCLES AND PHASE-SHIFT RATIO

In this section, the power transfer characteristic is studied for the unified control of duty cycles (D_1, D_2) and phase-shift ratio (Φ). The case when $\Phi < 0$ is not discussed since DAB dc–dc converter is symmetrical in view of the topology and control. Since the bias current is low, it is neglected in this section. Even though D_2 can be expressed by D_1 using (1), the power transfer is still controlled by two control variables including both D_1 and Φ. Optimized selection of D_1 and Φ should be made since there are numerous combinations of them for the same output power.

Fig. 6 presents the qualitative waveforms of three possible selections for the same output power transfer with TZM control.

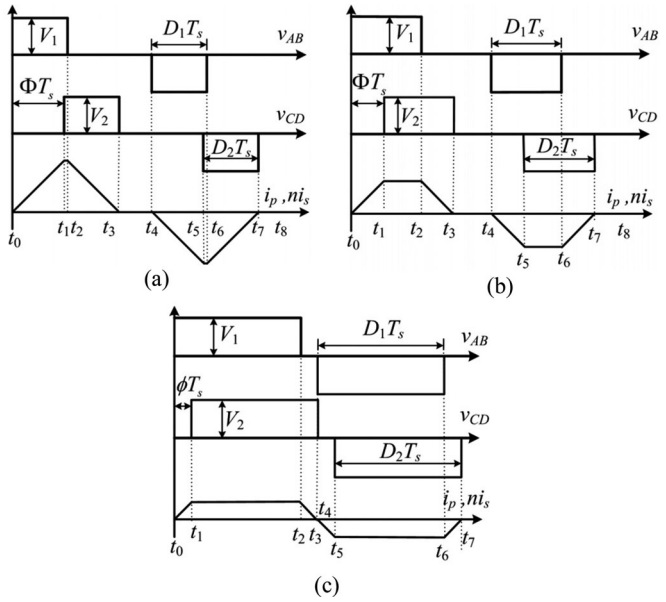

Fig. 6. Three conditions of D1 and Φ for the same power transfer with TZM control. (a) Small duty cycles and large Φ. (b) Middle duty cycles and middle Φ. (c) Small Φ and large duty cycles under critical continuous conduction mode.

During the interval $t_0 - t_1$, v_{CD} is zero. The transformer current does not contribute to the power transfer and only causes circulating current loss. Similarly, the circulating current loss also exists in the interval: $t_4 - t_5$. Compared with (a) and (b), the duration lengths of these intervals are the shortest in (c) and the maximum current is lowest, indicating lower rms current and lower circulating current loss.

A. Selections of Duty Cycles and Phase-Shift Ratio for Minimum RMS Circulating Current

As mentioned before, different control points of D_1 and Φ generate different current waveforms, leading to different peak currents and circulating losses. Therefore, it is necessary to optimize duty cycles and the phase ratio.

Mathematically, based on the waveform in Fig. 6, $i(t_1)$ and $i(t_2)$ can be written by, respectively

$$\begin{aligned} i(t_1) &= \int_{t_0}^{t_1} (V_1/L_k)dt = V_1 \Phi T_s / L_k \\ i(t_2) &= \int_{t_0}^{t_1} \frac{V_1}{L_k} dt + \int_{t_1}^{t_2} \frac{V_1 - V_2}{L_k} dt \\ &= \frac{V_2 T_s}{n L_k} \left(\Phi + \left(\frac{nV_1}{V_2} - 1 \right) D_1 \right). \end{aligned} \tag{24}$$

The rms circulating current in a switching period for one active bridge can be calculated as

$$\begin{aligned} I_{c\_\mathrm{rms}} &= \sqrt{\left(\int_{t_0}^{t_1} \left(\frac{V_1}{L_k} t \right)^2 dt + \int_{t_5}^{t_4} \left(\frac{V_1}{L_k} t \right)^2 dt \right) \Big/ T_s} \\ &= \frac{V_1 T_s}{L_k} \sqrt{\frac{2\Phi^3}{3}}. \end{aligned} \tag{25}$$

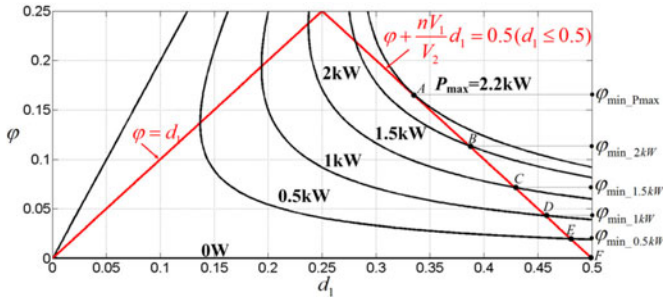

Fig. 7. Plot of φ versus d_1 for different output power ($V_1 = 200V, V_2 = 200V, n = 1, L_k = 30\mu H, f_s = 50kHz$).

Equations (24) and (25) indicate that small Φ results in lower circulating current and $i(t_1)$, causing low conduction loss and peak current. However, if Φ is too small, the power transfer may be limited since decreasing of Φ may reduce the output power. Thus, it is necessary to find the minimum Φ with the precondition of the ability to transfer the required power.

Let p, d_1, d_2, and φ denote the variables for the equilibrium values P, D_1, D_2, and Φ, respectively. Then, the power transfer function in (2) is

$$p(d_1, \varphi) = V_1 ({d_1}^2 V_1 - (d_1 - \varphi)^2 V_2 / n) / (L_k f_s). \tag{26}$$

According to the working principle of TZM control, the ranges for two duty cycles can be shown as

$$\varphi T_s < d_1 T_s < 0.5 T_s \cap \varphi T_s + d_2 T_s < 0.5 T_s. \tag{27}$$

Substitution of $d_1 V_1 = d_2 V_2 / n$ into (27) leads to

$$\varphi \le d_1 \le 0.5 \cap \varphi + n V_1 d_1 / V_2 \le 0.5. \tag{28}$$

For a given fixed power P_o, φ can be regarded as a function of d_1. Thus

$$\frac{\partial P_o}{\partial d_1} = \frac{\partial [V_1 ({d_1}^2 V_1 - (d_1 - \varphi)^2 V_2 / n) / (L_k f_s)]}{\partial d_1} = 0. \tag{29}$$

Simplification of (29) leads to

$$\frac{\partial \varphi}{\partial d_1} = \frac{d_1 (V_2 - n V_1) - \varphi V_2}{(d_1 - \varphi) V_2}. \tag{30}$$

If $V_1 \ge V_2/n$, $\partial\varphi/\partial d_1 < 0$,$\varphi$ is monotone decreasing with d_1. Therefore, minimum φ can be obtained at the boundary condition in (28). When $\varphi = d_1$, minimum φ cannot be got because $I_{p\max}$ and I_{c_rms} are both the largest as also illustrated in Fig. 6 (a). Therefore, the minimum φ for a given output power P_o exists at the boundary condition, which is described by

$$\varphi + n V_1 d_1 / V_2 = 0.5 (d_1 \le 0.5). \tag{31}$$

Fig. 7 shows an example for plot of φ versus d_1 for different output power when $V_1 = V_2$. As the output power changes from 0 to 2200 W, the point of minimum φ changes from point F to A and they all exist at the boundary, which agrees with the aforementioned analysis.

If $V_1 < V_2/n$, (30) is not a monotone decreasing function of d_1. The minimum point can be calculated by setting $\partial\varphi/\partial d_1 =$

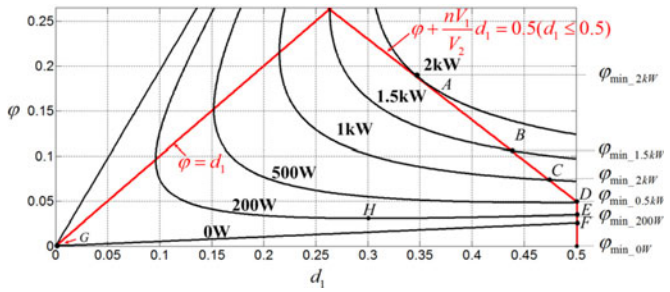

Fig. 8. Plot of φ versus d_1 for different output power ($V_1 = 180$ V, $V_2 = 200$ V, $n = 1$, $L_k = 30\ \mu$H, $f_s = 50$ kHz).

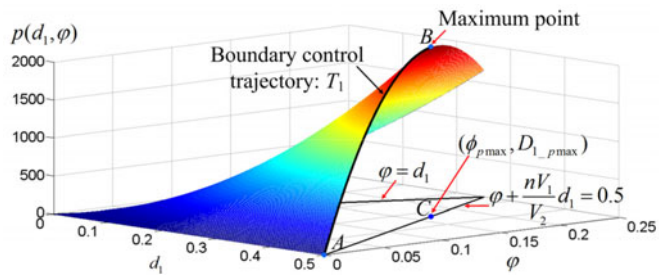

Fig. 9. Power transfer function curve ($V_1 = 200$ V, $V_2 = 200$ V, $n = 1$, $L_k = 30\ \mu$H, $f_s = 50$ kHz).

0. Then

$$\varphi_{\min} = d_{1\min}(V_2 - nV_1)/V_2. \tag{32}$$

Therefore, for a given power P_o, if $\varphi_{\min} + nV_1 d_{1\min}/V_2 > 0.5$, the minimum φ exists at the boundary condition: $\varphi + nV_1 d_1/V_2 = 0.5$; if $\varphi_{\min} + nV_1 d_{1\min}/V_2 < 0.5$, the minimum φ is $\varphi_{\min} = d_{1\min}(V_2 - nV_1)/V_2$.

Fig. 8 plots φ versus d_1 with different output power when $V_1 < V_2$ for one case. As seen, when the output power changes from 500 to 2000 W, the point of minimum φ also occurs at the boundary. When the power is relatively lower such as 0 or 200 W, the points of minimum φ are point *G* and point *H*, respectively. But the boundary points for the two output power plots occur at point *F* and point *E*. In this case, the boundary condition is not suitable for achieving minimum φ. However, the calculation for $\varphi_{\min}$ and $d_{1\min}$ is complex, and the difference of φ between the point *H* and *E* (or *G* and *F*) is very small. Therefore, when $V_1 < V_2/n$ at light load, the boundary condition can still be used to select D_1 and Φ to simply the calculation at the cost of slightly increased circulating current and rms value.

B. Maximum Power Transfer Point

To investigate the combination of D_1 and Φ for maximum power transfer, the following function is defined as

$$\varphi + nV_1 d_1/V_2 = a, (0 \le a \le 0.5). \tag{33}$$

When a changes from 0 to 0.5, this function can traverse all the existed point (d_1, φ) for the power transfer function in (26). Substitution of (33) into (26) and elimination of φ leads to

$$p(a, d_1) = \frac{V_1}{L_k f_s}({d_1}^2 V_1 - (d_1 - a + \frac{nV_1}{V_2} d_1)^2 \frac{V_2}{n}). \tag{34}$$

Then

$$\frac{\partial p(a, d_1)}{\partial d_1} = \frac{2V_1}{nV_2 L_k f_s}(-({V_2}^2 + n^2 {V_1}^2 + nV_1V_2)d_1 + ({V_2}^2 + nV_1V_2)a). \tag{35}$$

Let $\partial p(a, d_1)/\partial d_1 = 0$, since $-({V_2}^2 + n^2{V_1}^2 + 2nV_1V_2) < 0$, the maximum power transfer occurs at the point when

$$d_{1\_p\max}(a) = \frac{({V_2}^2 + nV_1V_2)}{({V_2}^2 + n^2{V_1}^2 + nV_1V_2)} a, (0 < a \le 0.5). \tag{36}$$

Substitution of (36) into (33) yields

$$\varphi_{p\max}(a) = \frac{V_2}{V_2 + nV_1} d_{1\_p\max} = \frac{{V_2}^2}{({V_2}^2 + n^2{V_1}^2 + nV_1V_2)} a. \tag{37}$$

Then, substitution of (36), (37) into (34) yields

$$p_{\max}(a) = V_1({d_{1\_p\max}}^2 V_1 - (d_{1\_p\max} - \varphi_{p\max})^2 V_2/n)/(L_k f_s) = \frac{V_1^2}{L_k f_s} \frac{V_2^4 + n^2 V_1^2 V_2^2 + nV_1V_2^3}{(V_2^2 + n^2V_1^2 + nV_1V_2)^2} a^2, \quad (0 < a \le 0.5). \tag{38}$$

$p_{\max(a)}$ is a quadratic function of a, and its maximum value exists when $a = 0.5$. Therefore, the global maximum value of $p(d_1, \varphi)$ is

$$P_{\max}(0.5) = \frac{V_1^2}{4L_k f_s} \frac{{V_2}^4 + n^2{V_1}^2{V_2}^2 + nV_1{V_2}^3}{({V_2}^2 + n^2{V_1}^2 + nV_1V_2)^2} \tag{39}$$

and the corresponding $D_{1\_p\max}$ and $\phi_{p\max}$ are, respectively, expressed as

$$D_{1\_p\max} = \frac{({V_2}^2 + nV_1V_2)}{2({V_2}^2 + n^2{V_1}^2 + nV_1V_2)}$$
$$\phi_{p\max} = \frac{{V_2}^2}{2({V_2}^2 + n^2{V_1}^2 + nV_1V_2)}. \tag{40}$$

Note that $D_{1\_p\max}$ and $\phi_{p\max}$ satisfy the boundary condition in (31), which indicates that the maximum power occurs at the boundary.

IV. Boundary TZM Control and Its Implementation

A. Boundary TZM Control

As discussed in part *A* of Section III, the control point with lower rms current and circulating loss for an arbitrary given power occurs mostly at the boundary condition, and the maximum power point also exists at the boundary as mentioned in part *B* of Section III. If this boundary condition is used for the control of d_1 and φ, two advantages can be obtained. One is that the conduction loss can be reduced; the other is that the maximum power transfer will not be limited as the global maximum power point exists at the boundary condition.

The curve of $p(d_1, \varphi)$ is plotted in Fig. 9. As illustrated, the maximum point exists at the boundary that agrees with the mathematical calculation in Section III. Meanwhile, the boundary control trajectory T_1 is shown. This trajectory starts from

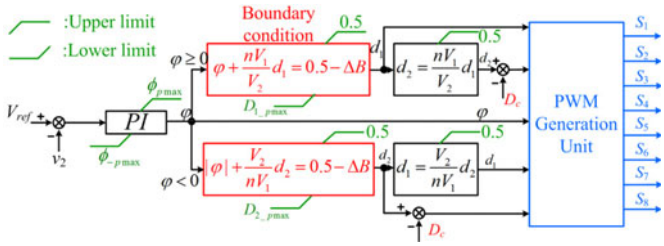

Fig. 10. Implementation of the boundary control using a PI regulator.

the minimum point *A* and ends at the maximum point *B*. It cannot run across point *B* because only one point should exist for the same output power, namely the control trajectory should be monotonous. As a result, the range for φ with the boundary condition can be obtained as

$$0 \le \varphi \le \phi_{p\max} \tag{41}$$

and the corresponding value range of d_1 is

$$D_{1\_p\max} \le d_1 \le 0.5 \tag{42}$$

where expressions of $D_{1\_p\max}$ and $\phi_{p\max}$ are shown in (40).

If φ is controlled through a *PI* regulator, based on the boundary condition and the value ranges in (41) and (42), d_1 can be obtained. Then, if d_1 is substituted into (1) d_2 can be calculated. Therefore, the optimized control for the power transfer can be realized by regulating the variable φ to achieve real time control.

B. Implementation of Boundary TZM Control

Fig. 10 shows the control diagram for the boundary TZM control. A PI regulator is used to control the voltage V_2 through control of φ. As shown, when $\varphi \ge 0$, the boundary condition is used to calculate d_1 and then d_2 is obtained based on (1). A small constant ΔB is added in the boundary condition to ensure the duration length of the bias currents, which can charge /discharge the junction capacitor to achieve ZVS. Hence, ΔBT_s should be larger than the minimum charging/discharging time t_c. When $\varphi < 0$, since the control principle is symmetrical, the boundary condition can be obtained by interchanging V_1 with V_2/n and replacing d_1 with d_2 in (31). Using this boundary condition, d_2 can be calculated, and then d_1 is also obtained based on (1). The PWM generation unit generates all the switching signals based on both the output of PI regulator (φ) and the calculated control variables (d_1 and d_2).

V. Experimental Verification

A laboratory prototype was built to validate the feasibility of the proposed ZVS method and unified boundary control strategy.

The initial parameters of the laboratory prototype are: 1) $V_1 = 180 - 240$ V, $V_2 = 200$ V; 2) turns ratio: 1:1; 3) rated power $P_o = 1.6$ kW; 4) switching frequency $f_s = 50$ kHz; e) IXFH69N30P is chosen as the power switches and its junction capacitor is 570 pF. Furthermore, the parameters including L_k, $I_{1\min}$, $I_{2\min}$, I_b, I_{bs}, D_c, and L_m are designed according to the following parameter design procedure.

1) Calculation of Inductor L_k

According to the maximum power transfer function in (39), L_k can be designed as

$$L_k \le \frac{{V_1}^2}{4f_s}\frac{{V_2}^4 + n^2{V_1}^2{V_2}^2 + nV_1{V_2}^3}{\left({V_2}^2 + n^2{V_1}^2 + nV_1V_2\right)^2 P_{o\max}}. \tag{43}$$

Here, $P_{o\max}$ is set as: $P_{o\max} = (1 + 20\%)\, P_o$ to ensure a 20% margin of the output power. Therefore, based on (43)

$$L_k \le 3.113 \times 10^{-5}(H). \tag{44}$$

The startup current of the converter decreases as L_k increases. L_k can be designed as large as it can be once (44) is satisfied. In this case, L_k is designed to be 30 μH.

2) Calculation of $I_{1\min}$, $I_{2\min}$

The switches junction capacitor is 570 pF. The minimum charging/discharging current for achieving ZVS within full input voltage range can be got according to Table I

$$\begin{aligned} \max(I_{1\,\min}) &= V_{1\_\max}\sqrt{2C_1/L_k} = 1.479(A) \\ I_{2\,\min} &= V_2\sqrt{2C_2/L_{ks}} = 1.233(A). \end{aligned} \tag{45}$$

3) Bias currents: I_b and I_{bs}

The current bias I_b of i_p in V_1 side does not change as the load varies. It is set as $(1 + 20\%) \cdot \max(I_{1\,\min})$ to obtain a 20% margin of the charging/discharging current for achieving ZVS of S_1 and S_2 within full input voltage range. However, the bias current I_{bs} of i_s in V_2 side is affected by the output power. Therefore, the minimum value of I_{bs}, which is denoted as $I_{bs\_\min}$, should be larger than the minimum charging/discharging current $I_{2\min}$ with also a 20% margin. These two parameters can be written as

$$\begin{cases} I_b = (1 + 20\%) \cdot \max(I_{1\,\min}) = 1.775 \approx 1.8(A) \\ I_{bs\_\min} = (1 + 20\%) I_{2\,\min} = 1.479 \approx 1.5(A) \end{cases}. \tag{46}$$

4) Duty cycle compensation value: D_c

Once L_k and I_b are certain, D_c can be obtained according to (15)

$$D_c = 2nL_k f_s I_b / V_2 = 0.027. \tag{47}$$

5) Magnetization inductance: L_m

When the boundary condition is applied, the transferred power p versus D_1 is written by

$$p(D_1) = \frac{V_1}{L_k f_s}\left({D_1}^2 V_1 - \left(D_1 + \frac{nV_1}{V_2}D_1 - 0.5\right)^2 V_2/n\right). \tag{48}$$

As discussed in part A of Section IV, the D_1 range is shown in (42) and the minimum value of D_1 is got at the highest transferred power. Assume $P\,(D_1) = P_o = 1600$, and solution of D_1 when $V_1 = 180$ and $V_1 = 240V$ leads to the minimum

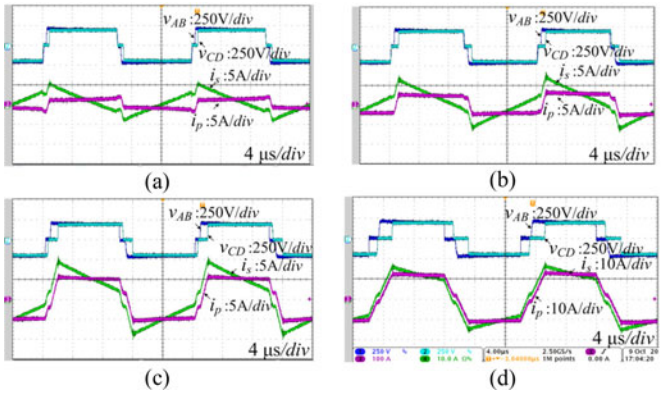

Fig. 11. Different load under $V_1 = V_2 = 200V$ condition (a) 200 W. (b) 400 W. (c) 800 W. (d) 1600 W.

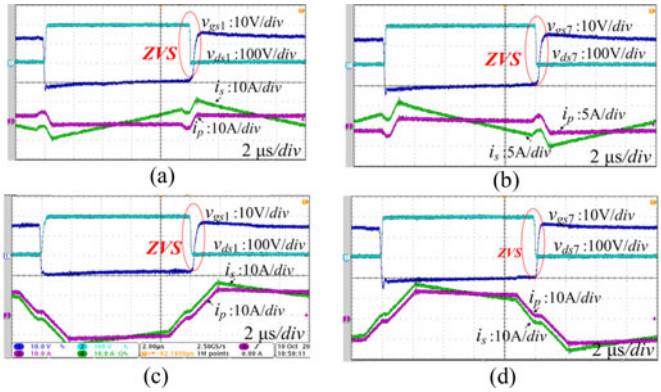

Fig. 12. ZVS under different loads ($V_1 = V_2 = 200$ V). (a) ZVS of S_1 under 200 W. (b) ZVS of S_7 under 200 W. (c) ZVS of S_1 under 1600 W. (d) ZVS of S_7 under 1600 W.

value of D_1

$$D_{1\_\min} = \begin{cases} 0.397 & \text{when} \quad V_1 = 240\,\text{V} \\ 0.436 & \text{when} \quad V_1 = 180\,\text{V} \end{cases}. \tag{49}$$

Since $0.397 \times 240 > 0.442 \times 180 = 79.56$, the minimum value of $D_1 \times V_1$ exists in the case when $V_1 = 180$ V and the minimum value is 79.56.

Meanwhile, based on (22), expression of the bias current I_{bs} can be written as

$$I_{bs} = V_2 D_2 T_s/(2n^2 L_m) - I_b/n. \tag{50}$$

L_m should be designed to make I_{bs} always larger than $I_{bs\_\min}$ to achieve ZVS. Thus, the following must be met:

$$\min(I_{bs}) = \min(V_1 D_1)/2nL_m f_s - I_b/n \geq I_{bs\_\min}. \tag{51}$$

Therefore, L_m should be calculated as

$$L_m \leq \min(V_1 D_1)/(2(I_b + nI_{bs\_\min})f_s) = 2.411 \times 10^{-4}(H). \tag{52}$$

Since decrease of L_m leads to higher peak current and RMS current in V_2 side, L_m should be designed as large as possible once (52) is satisfied. Therefore, in this case, $\mathrm{L_m}$ is 240 μH.

The experimental results of different loads under $V_1 = V_2 = 200$ V condition are shown in Fig. 11. As seen, the two bias currents, which are properly designed by the fixed duty cycle compensation and magnetizing current design, occur at the boundary when both v_{AB} and v_{CD} are zero to create ZVS conditions for the aforementioned four switches. These two bias currents always exist despite the load. Under 200-W load condition, as shown in Fig. 11(a), the duty cycles of v_{AB} and v_{CD} are the largest compared with other conditions. Besides, the duty cycles of v_{AB} and v_{CD} decrease while the phase-shift ratio increases, which agrees with the analysis. Furthermore, as seen from the current waveforms, the transformer currents are always critical continuous for different loads if the two bias currents are neglected.

The ZVS when $V_1 = V_2 = 200$ V is shown in Fig. 12. Switches S_1 and S_7 are chosen to show the effectiveness of the proposed control. v_{gs} is the driver signals, and v_{ds} is the drain to source voltages. As shown in all the figures, ZVS can be obtained under both light load and full load.

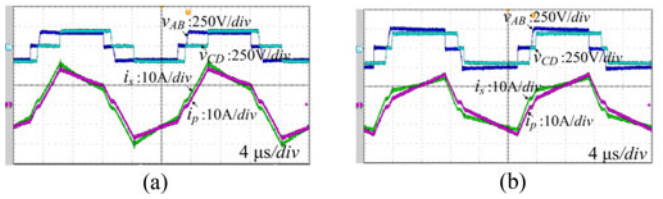

Fig. 13. Different input voltage under rated load condition. (a) 180-V input. (b) 240-V input.

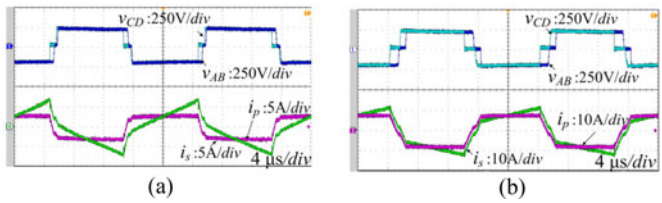

Fig. 14. Experimental waveforms when the power transfers backward from V_2 to V_1 under rated input voltage. (a) 400-W reverse power flow. (b) 1200-W reverse power flow.

Fig. 13 shows different input voltages under rated load condition. As illustrated, the two bias currents also occur at the boundary and can be used to achieve ZVS as seen from the waveforms of v_{AB} and v_{CD}. Although the input and output voltage are not matched, the transformer current remains critical continuous if the two bias currents are ignored. This implies that the boundary condition can be ensured under different input voltages.

The experimental waveforms in reverse power flow under 400 and 1200 W conditions are shown in Fig. 14. As seen, v_{AB} lags v_{CD}, indicating that the phase-shift ratio becomes negative to achieve reverse power flow. Meanwhile, the two currents also remain critical continuous if the two bias currents are neglected, which shows the proposed control is also effective in reverse power flow condition. Meanwhile, no voltage spike or ringing occurs in v_{AB} and v_{CD}, indicating ZVS.

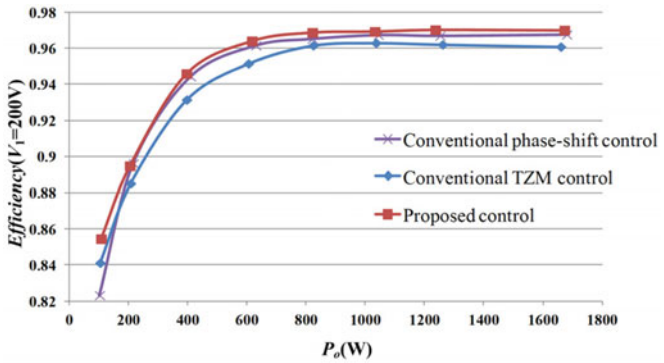

Fig. 15. Efficiency comparison when $V_1 = 200$ V.

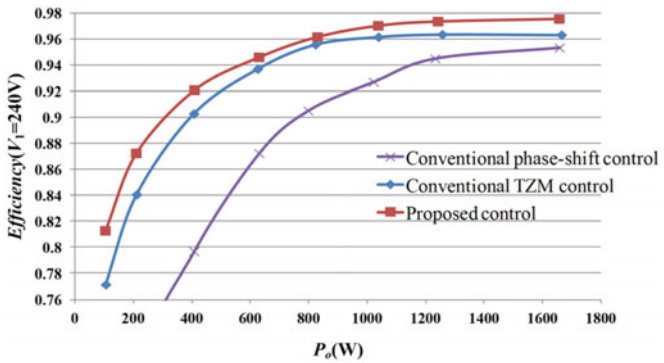

Fig. 16. Efficiency comparison when $V_1 = 240$ V.

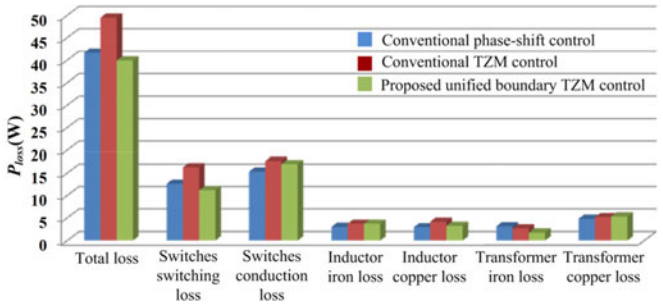

Fig. 17. Comparisons of the calculated power loss breakdown at the rated load when $V_1 = 200$ V.

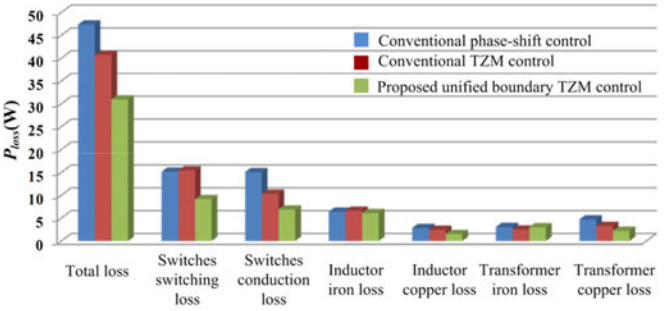

Fig. 18. Comparisons of the calculated power loss breakdown at the rated load when $V_1 = 240$ V.

The efficiency of the converter with the proposed control method is measured and compared with the one using the CPS control and the conventional TZM control. In Fig. 15, $V_1 = 200$ V, which matches with the voltage in V_2 side. In this case, with the conventional TZM control, the efficiency is relatively lower because ZVS is lost for four power switches. Meanwhile, the proposed converter efficiency is slightly higher than the one with CPS control at heavy load due to very low turn off current for four power switches. When $V_2 = 240$ V as shown in Fig. 16, the efficiency of the converter with CPS control decreases significantly due to high-peak current, large nonactive power and losing of ZVS. Besides, compared with conventional TZM control, the efficiency with the proposed control has an improvement of 4% at light load (100 W) and the improvement at the heavy load is roughly 1.5%.

Figs. 17 and 18 show the loss breakdown of the converter with the three control methods under rated power when $V_1 = 200$ V and $V_1 = 240$ V. As shown in Fig. 17, when the voltages of V_1 side and V_2 side are matched, the conventional TZM can lead to more loss due to higher switches switching loss and switches conduction loss. In this case, the total power loss of the system with the proposed control is slightly lower than the one with the CPS control because of lower switches switching loss. The total power loss difference between them is small since ZVS of all the eight power switches can also be achieved for CPS control when the voltages of V_1 side and V_2 side are matched. However, the total power loss difference between the CPS control and proposed control becomes larger when $V_1 = 240$ V, as shown in Fig. 18. In this case, the switches peak current and circulating current are both increased for the CPS control, leading to higher switches switching loss and conduction loss compared with the proposed control. Meanwhile, compared with the conventional TZM control, the proposed control has less switches loss and copper loss since the boundary condition is applied and ZVS of all the switches can be ensured with the fixed duty cycle compensation and magnetizing current design.

VI. Conclusion

This paper proposes a unified boundary TZM control for dual active bridge dc–dc converters. It utilizes the proposed fixed duty cycle compensation and magnetizing current design to achieve ZVS for all switches. With the proposed control, the selection of control variables for the power transfer is unified and can be implemented by one regulator. Besides, the converter has no nonactive power issues if the two low bias currents are ignored. Using the introduced boundary control, the conduction loss can be further reduced because of no nonactive power and lower circulating current. The fixed duty cycle compensation and the magnetizing current design can achieve ZVS for the left four power switches, which cannot be obtained with the conventional TZM control. As a result, all the power switches can achieve ZVS and half of the switches can be turned OFF with ZCS if the small bias current is ignored. Experimental results from 1.6-kW laboratory prototypes have verify the theoretical analysis and the effectiveness of the proposed control.

REFERENCES

[1] R. W. A. A. De Doncker, D. M. Divan, and M. H. Kheraluwala, "A three phase soft-switched high-power-density dc/dc converter for high-power applications," *IEEE Trans. Ind. Appl.*, vol. 27, no. 1, pp. 63–73, Jan./Feb. 1991.

[2] M. N. Kheraluwala, R. W. Gascoigne, D. M. Divan, and E. D. Baumann, "Performance characterization of a high-power dual active bridge dc-to-dc converter," *IEEE Trans. Ind. Appl.*, vol. 28, no. 6, pp. 1294–1301, Nov./Dec. 1992.

[3] S. Inoue and H. Akagi, "A bidirectional dc–dc converter for an energy storage system with galvanic isolation," *IEEE Trans. Power Electron.*, vol. 22, no. 6, pp. 2299–2306, Nov. 2007.

[4] H. Bai, C. C. Mi, and S. Gargies, "The short-time-scale transient processes in high-voltage and high-power isolated bidirectional dc–dc converters," *IEEE Trans. Power Electron.*, vol. 23, no. 6, pp. 2648–2656, Nov. 2008.

[5] D. Costinett, D. Maksimovic, and R. Zane, "Design and control for high efficiency in high step-down dual active bridge converters operating at high switching frequency," *IEEE Trans. Power Electron.*, vol. 28, no. 8, pp. 3931–3940, Aug. 2013.

[6] G. Oggier, G. O. Garci, and A. R. Oliva, "Modulation strategy to operate the dual active bridge dc–dc converter under soft switching in the whole operating range," *IEEE Trans. Power Electron.*, vol. 26, no. 4, pp. 1228–1236, Apr. 2011.

[7] H. Bai and C. Mi, "Eliminate reactive power and increase system efficiency of isolated bidirectional dual-active-bridge dc–dc converters using novel dual-phase-shift control," *IEEE Trans. Power Electron.*, vol. 23, no. 6, pp. 2905–2914, Nov. 2008.

[8] G. D. Demetriades and H. P. Nee, "Characterization of the dual-active bridge topology for high-power applications employing a duty-cycle modulation," in *Proc. IEEE Power Electron. Spec. Conf.*, 2008, pp. 2791–2798.

[9] G. G. Oggier, G. O. Garcia, and A. R. Oliva, "Switching control strategy to minimize dual active bridge converter losses," *IEEE Trans. Power Electron.*, vol. 24, no. 7, pp. 1826–1838, Jul. 2009.

[10] B. Zhao, Q. Yu, and W. Sun, "Extended-phase-shift control of isolated bidirectional dc–dc converter for power distribution in microgrid," *IEEE Trans. Power Electron.*, vol. 27, no. 11, pp. 4667–4680, Nov. 2012.

[11] B. Zhao, Q. Song, and W. Liu, "Power characterization of isolated bidirectional dual-active-bridge dc–dc converter with dual-phase-shift control," *IEEE Trans. Power Electron.*, vol. 27, no. 9, pp. 4172–4176, Sep. 2012.

[12] H. Bai, Z. Nie, and C. C. Mi, "Experimental comparison of traditional phase-shift, dual-phase-shift, and model-based control of isolated bidirectional dc–dc converters," *IEEE Trans. Power Electron.*, vol. 25, no. 6, pp. 1444–1449, Jun. 2010.

[13] F. Krismer and J. W. Kolar, "Accurate small-signal model for the digital control of an automotive bidirectional dual active bridge," *IEEE Trans. Power Electron.*, vol. 24, no. 12, pp. 2756–2768, Dec. 2009.

[14] F. Krismer and J. W. Kolar, "Efficiency-optimized high-current dual active bridge converter for automotive applications," *IEEE Trans. Ind. Electron.*, vol. 59, no. 7, pp. 2745–2760, Jul. 2012.

[15] K. Wu, C. W. de Silva, and W. G. Dunford, "Stability analysis of isolated bidirectional dual active full-bridge dc–dc converter with triple phase shift control," *IEEE Trans. Power Electron.*, vol. 27, no. 4, pp. 2007–2017, Apr. 2012.

[16] Y. A. Harrye, K. H. Ahmed, and A. A. Aboushady, "Reactive power minimization of dual active bridge DC/DC converter with triple phase shift control using neural network", in *Proc. Int. Conf. Renewable Energy Res. Appl.*, 2014, pp.566–571.

[17] H. Wen, W. Xiao, and B. Su, "Nonactive power loss minimization in a bidirectional isolated dc–dc converter for distributed power systems," *IEEE Trans. Ind. Electron.*, vol. 61, no. 12, pp. 6822–6831, Dec. 2014.

[18] N. Schibli, "DC–DC converter for two-quadrant operation with controlled output voltage," in *Proc. Eur. Conf. Power Electron. Appl.*, Lausanne, Switzerland, Sep. 1999, pp. 1–8.

[19] F. Krismer, S. Round, and J. W. Kolar, "Performance optimization of a high current dual active bridge with a wide operating voltage range," in *Proc. 37th IEEE Power Electron. Spec. Conf.*, Jun. 2006, pp. 1–7.

[20] T. Hirose, M. Takasaki, and Y. Ishizuka, "A power efficiency improvement technique for a bidirectional dual active bridge dc–dc converter at light load," *IEEE Trans. Ind. Appl.*, vol. 50, no. 6, pp. 4047–4055, Nov./Dec. 2014

[21] H. Zhou and A. M. Khambadkone, "Hybrid modulation for dual-active bridge bidirectional converter with extended power range for ultra capacitor application," *IEEE Trans. Ind. Appl.*, vol. 45, no. 4, pp. 1434–1442, Jul./Aug. 2009.

Guo Xu (S'15) received the B.S. degree in electrical engineering and automation from the Beijing Institute of Technology, Beijing, China, in 2012, where he is currently working toward the Ph.D. degree in electrical automation.

His research interests include modeling and control of power electronics converters and high power density converters.

Deshang Sha (M'09) received the B.S. degree from the Luoyang Institute of Technology, Luoyang, China, in 1998, the M.S. degree from the Nanjing University of Aeronautics and Astronautics, Nanjing, China, in 2001, and the Ph.D. degree from the Institute of Electrical Engineering, Chinese Academy of Sciences, Beijing, China, in 2005, all in electrical engineering.

From 2005 to 2007, he was a Chief Engineer of the Full-Digitalized Welding Machine Research Department, Time Group Inc., Beijing. Since 2008, he has been with the School of Automation, Beijing Institute of Technology, Beijing, where he is currently an Associate Professor. From 2012 to 2013, he was a Visiting Scholar with the Future Energy Electronics Center, Virginia Tech, Blacksburg, VA, USA. His current research interests include high-efficiency power conversion and power electronics applications in microgrid systems.

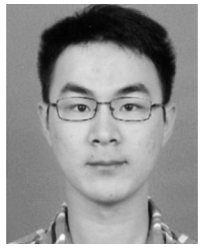

Jiankun Zhang received the B.S. degree from Beijing Institute of Technology (BIT), Beijing, China, in 2014, where he is currently working toward the M.S. degree in electrical engineering.

His research interest includes dc/dc converters and dc/ac inverters.

Xiaozhong Liao (M'09) received the B.S. and M.S. degrees in electrical engineering from Tianjin University, Tianjin, China, in 1982 and 1984, respectively, and the Ph.D. degree in control sciences and engineering from the Beijing Institute of Technology, Beijing China, in 2004.

She was a Visitor Researcher in the Department of Electrical and Electronic Engineering, University of Central Lancashire, Preston, U.K., from 1995 to 1996. She is currently an Associate Dean and Full Professor in the School of Automation, Beijing Institute of Technology. Her current research interests include power electronics, motor drives, and renewable energy power conversion.